Joint Inversion of Geophysical Data for Geologic Carbon Sequestration Monitoring: A Differentiable Physics-Informed Deep Learning Model

Mingliang Liu[1], Dario Grana[2] and **Tapan Mukerji[1]**

[1] Department of Energy Resources Engineering, Stanford University, USA.

[2] Department of Geology and Geophysics, University of Wyoming, USA.

Corresponding author: Mingliang Liu (mliu9@stanford.edu)

Key Points:

- A novel inverse model is developed by combining differentiable physics and deep neural networks
- The developed model provides an accurate and efficient approach for the joint inversion of geophysical data from different sources
- The inverted models accurately characterize subsurface properties and structures and identify the migration of CO_2 plume

ABSTRACT

Geophysical monitoring of geologic carbon sequestration is critical for risk assessment during and after carbon dioxide (CO_2) injection. Integration of multiple geophysical measurements is a promising approach to achieve high-resolution reservoir monitoring. However, joint inversion of large geophysical data is challenging due to high computational costs and difficulties in effectively incorporating measurements from different sources and with different resolutions. This study develops a differentiable physics model for large-scale joint inverse problems with reparameterization of model variables by deep neural networks and implementation of a differentiable programming approach of the forward model. The main novelty is the use of automatic differentiation and parallel computing for efficient multiphysics data assimilation. The application to the Sleipner benchmark model demonstrates that the proposed method is effective in estimation of reservoir properties from seismic and resistivity data and shows promising results for CO_2 storage monitoring.

Plain Language Summary

This study develops a complete inversion model for the joint quantification and interpretation of geophysical measurements from different sources for geologic carbon sequestration monitoring. By combining deep neural networks for model reparameterization and differentiable programming for inverse modeling, the developed approach accurately characterizes subsurface reservoirs, it identifies the migration of CO_2 plume, and it quantifies global parameters that are uncertain in the forward models. One of the major advantages of this method is that all components in the model are seamlessly integrated and updated simultaneously. Moreover, the model can be easily deployed to high-performance computing platforms, thereby providing a computationally efficient approach for large geophysical data. Therefore, the developed model illustrates promising results for geophysical subsurface monitoring.

1. Introduction

Geologic CO_2 sequestration (GCS) is one of the main mitigation strategies to prevent carbon dioxide (CO_2) from entering the atmosphere by capturing and injecting it into subsurface geological formations, such as depleted oil reservoirs and deep saline aquifers (Metz et al. 2005; Aminu et al. 2017). To ensure safe and long-term CO_2 storage, geophysical monitoring surveys are periodically acquired to surveil the behavior of the injected CO_2 and make informed decisions for storage management (Davis et al., 2019).

Time-lapse (4-D) seismic data is one of the monitoring techniques widely deployed in GCS projects, where a series of seismic surveys are sequentially acquired to quantify changes in reservoir properties (e.g., elastic properties, fluid pressure and saturation) during and after CO_2 injection (Chadwick et al., 2010; Caspari et al., 2011; Rubino et al., 2011; Grude et al., 2013; Egorov et al., 2017; Glubokovskikh et al., 2020; Li and Li, 2021). However, in some cases, depending on the rock stiffness, the time-lapse seismic response might be insensitive to fluid changes. (Gasperikova et al., 2022). To address this issue, non-seismic monitoring techniques have been investigated and successfully applied to GCS. For example, interferometric synthetic-aperture radar (InSAR) is an effective tool for measuring reservoir surface displacements and to infer reservoir pressure changes (Tang et al., 2022). Time-lapse gravity data are sensitive to bulk density, hence mass balance changes due to CO_2 injection (Bonneville et al., 2022). Electromagnetic (EM) and electrical techniques are used to estimate CO_2 saturation because of the distinct resistivity differences between brine- and CO_2-saturated rocks (Bhuyian et al., 2012). The spatial resolution of non-seismic surveys, however, is generally lower than the resolution of seismic surveys. Joint time-lapse monitoring of seismic and non-seismic measurements is then a potential approach to achieve high-resolution reservoir monitoring and

reduce the uncertainty. This approach has been used in hydrocarbon exploration but it is relatively new for GCS monitoring. Eliasson et al. (2014) investigated the integration of controlled-source electromagnetic (CSEM) inversion with full waveform seismic inversion for CO_2 quantification. Dupuy et al. (2021) developed a Bayesian joint inversion method for CO_2 storage monitoring with uncertainty quantification. Huang (2022) comprehensively reviewed the advantages and limitations of different geophysical techniques and their applications in long-term GCS monitoring.

The main challenge of joint geophysical monitoring is how to efficiently assimilate geophysical measurements from different sources. In general, joint geophysical inversion methods can be categorized into sequential or simultaneous schemes (Tveit et al., 2020). The sequential scheme inverts geophysical measurements in separate steps with the resulting model from one measurement as initial model or constraint for the next step, while the simultaneous scheme inverts all measurements in a single step. In the sequential scheme, measurements with lower resolution are generally inverted first, such that low frequency models are used as initial models for the inversion of higher resolution datasets. In the simultaneous scheme, model parameters are coupled with structural or rock-physics constraints and the forward operator includes multi-physics models. For this reason, simultaneous schemes are preferred to sequential schemes despite the higher computational complexity.

Recently, scientific machine learning (SciML) is getting increasing attention in the geophysics community, especially for its ability to address the computational challenges in large-scale geophysical inverse problems. These approaches mainly involve physics-informed neural networks (PINNs) (Raissi et al., 2019; Rasht-Behesht et al., 2022) and differentiable physics (Hernández et al., 2022). PINNs embed the governing physics laws (i.e., partial differential

89 equations) into deep neural networks (DNNs) as prior information to overcome the issue of
90 limited data, bridging the gap between the data scarcity of inverse problems and data
91 requirements of DNNs. PINNs are a mesh-free method that is theoretically advantageous for
92 high-dimensional problems. However, PINNs still face difficulties of training and convergence
93 in practice due to the lack of information about connectivity between neighboring points (or
94 nodes). Differentiable physics provides an alternative approach for physics modeling by
95 integrating differentiable programming with classical numerical methods (e.g., finite difference
96 method and finite element method). Differentiable programming is a new programming
97 paradigm in which all numerical operations are implemented by differentiable building blocks.
98 Such differentiable mechanism enables solving the forward and inverse problems via automatic
99 differentiation and can be easily combined with DNNs. Differentiable programming has been
100 applied in geophysics, such as geostatistical seismic inversion (Liu and Grana, 2019), full
101 waveform inversion (Zhu et al., 2022) and subsurface flow problems (Li et al., 2020).
102 To address the computational challenges in geophysical CO_2 monitoring, we propose a
103 differentiable physics model that assimilates time-lapse seismic and resistivity data to predict
104 porosity and the evolution of CO_2 saturation over time. In this approach, large geological models
105 are represented by a DNN with fewer parameters than the actual model and geophysical forward
106 operators are implemented using the differentiable programming framework. We also use a
107 Bayesian neural network (BNN) to estimate global parameters that are uncertain in the forward
108 physics model. By adopting automatic differentiation and graphics processing unit (GPU), model
109 parameters are automatically updated in a computationally efficient manner to minimize the
110 mismatch between predicted and true measurements.
111

2. Methods

In this study, we focus on joint inversion of time-lapse pre-stack seismic and resistivity data, with the goal of predicting porosity and the evolution of CO_2 saturation over time. Seismic data are linked to the reservoir properties (i.e., porosity and fluid saturations) through rock physics models, e.g., the unconsolidated sand model (Dvorkin and Nur, 1996) and convolution-based seismic wave propagation model (Yilmaz, 2001), whereas resistivity is linked to porosity and saturation through empirical equations, e.g., Archie's law (Archie, 1942). Rock physics parameters, such as coordination number and critical porosity in the unconsolidated sand model and the cementation and saturation exponents in Archie's law, are often uncertain in practical applications; hence, we assume that those rock physics parameters are unknown global model parameters. The proposed differentiable physics inversion is illustrated in Figure 1a. The global model parameters (coordination number, critical porosity, and cementation and saturation exponents) and reservoir model spatial variables (porosity and CO_2 saturations) are re-parameterized by a BNN and a convolutional neural network (CNN), respectively. Then, time-lapse seismic and resistivity data are predicted from the output model parameters of the neural networks through the forward models implemented by differentiable programming. With the technique of automatic differentiation, the network parameters are iteratively updated to minimize the loss function. After training, the inverted global parameters and reservoir properties can be obtained as the outputs of the trained BNN and CNN, respectively.

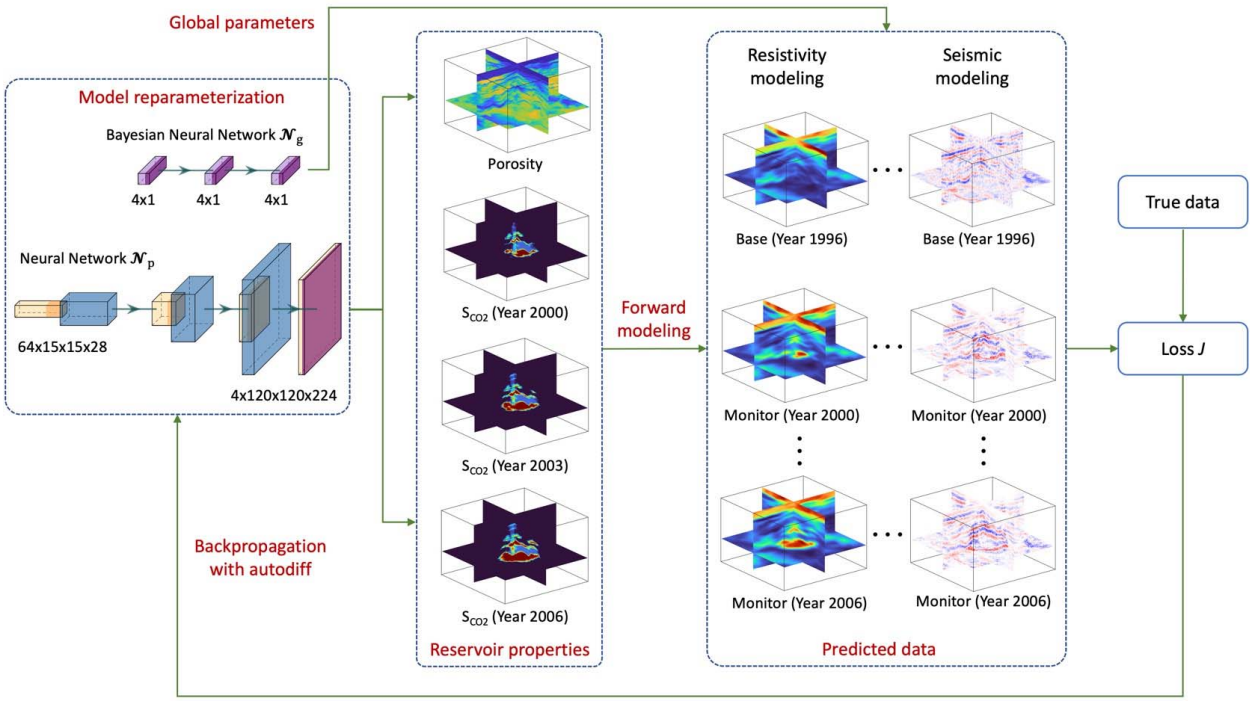

(a)

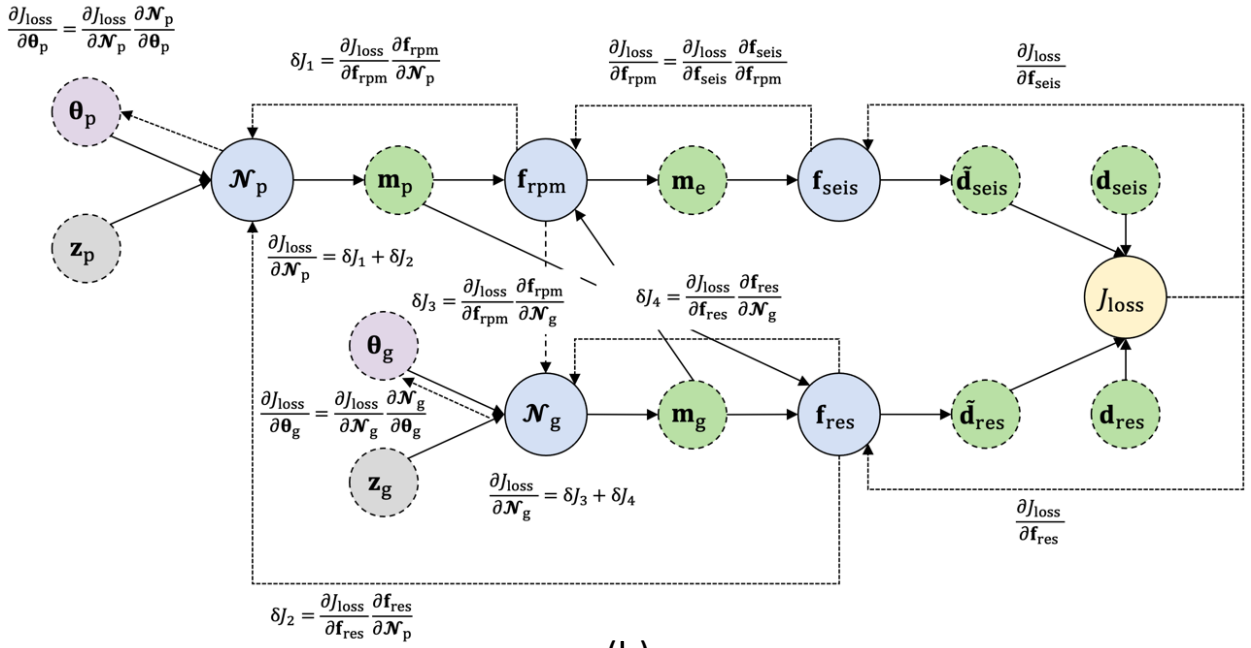

(b)

Figure 1. (a) Workflow of complete differentiable physics model for joint geophysics inversion; (b) Data Flow Graph corresponding to the workflow. Circles with solid and dashed line represent operators and variables, respectively. Purple circles ($\boldsymbol{\theta}_g$ and $\boldsymbol{\theta}_p$) represent the learnable neural network parameters and

gray circles ($\mathbf{z}_g$ and $\mathbf{z}_p$) represent constant inputs (latent vectors) that are non-trainable. Other symbols and notations are defined in Section 2.

2.1 Forward Modeling

The forward operator for the prediction of the seismic response includes a rock physics model that maps petrophysical properties (porosity and water saturation) to elastic properties (P- and S-wave velocity and density) and a convolution-based seismic wave propagation model that computes seismic travel time and reflection amplitudes. The mathematical-physical equation of the forward seismic model is expressed symbolically as follows

$$\mathbf{d}_{\text{seis}} = \mathbf{f}_{\text{seis}}\left(\mathbf{f}_{\text{rpm}}\left(\mathbf{m}_g, \mathbf{m}_p\right)\right) + \boldsymbol{\epsilon}_{\text{seis}}, \quad (1)$$

where $\mathbf{d}_{\text{seis}}$ represents the predicted seismic data, $\mathbf{m}_g$ represents the global model parameters (coordination number, and critical porosity), $\mathbf{m}_p$ represents the spatially-varying petrophysical properties (porosity and water saturation), $\mathbf{f}_{\text{rpm}}$ is the rock physics model for the prediction of elastic properties $\mathbf{m}_e$, $\mathbf{f}_{\text{seis}}$ is the seismic wave propagation model, and $\boldsymbol{\epsilon}_{\text{seis}}$ represents the measurement errors. The rock physics model adopted in this study is the unconsolidated sand model (Dvorkin and Nur, 1996). The detailed descriptions of the unconsolidated sand model and the convolution-based seismic wave propagation model can be found in Appendix A and B, respectively.

The forward operator for resistivity is Archie's law (Archie, 1942), that calculates the electrical resistivity of reservoir rocks $\mathbf{d}_{\text{res}}$ as a function of $\mathbf{m}_g$ and $\mathbf{m}_p$

$$\mathbf{d}_{\text{res}} = \mathbf{f}_{\text{res}}\left(\mathbf{m}_g, \mathbf{m}_p\right) = \boldsymbol{\phi}^{-m} R_w \mathbf{S}_w^{-n} + \boldsymbol{\epsilon}_{\text{res}}, \quad (2)$$

where $\mathbf{f}_{\text{res}}$ is the electrical rock physics model (Archie's law), the cementation m and saturation exponent n are two empirical parameters, $\mathbf{m}_p$ includes porosity $\boldsymbol{\phi}$ and water saturation $\mathbf{S}_w$,

while $\boldsymbol{\epsilon}_{\mathrm{res}}$ is the associated error. Here we assume that CO_2 saturation $\mathbf{S}_{\mathrm{CO2}} = 1 - \mathbf{S}_{\mathrm{w}}$ and the resistivity of the brine R_{w} is known and constant.

In the following example, we introduce measurement error ($\boldsymbol{\epsilon}_{\mathrm{seis}}$ and $\boldsymbol{\epsilon}_{\mathrm{res}}$) to the "true" seismic ($\mathbf{d}_{\mathrm{seis}}$) and resistivity ($\mathbf{d}_{\mathrm{res}}$) measurements to avoid the "inversion crime" and discard the error terms when predicting data ($\tilde{\mathbf{d}}_{\mathrm{seis}}$ and $\tilde{\mathbf{d}}_{\mathrm{res}}$) from inverted models.

2.2 Model Reparameterization

Two neural networks ($\boldsymbol{\mathcal{N}}_{\mathrm{g}}$ and $\boldsymbol{\mathcal{N}}_{\mathrm{p}}$) are used for the reparameterization of the global $\mathbf{m}_{\mathrm{g}}$ and petrophysical parameters $\mathbf{m}_{\mathrm{p}}$:

$$\mathbf{m}_{\mathrm{g}} = \boldsymbol{\mathcal{N}}_{\mathrm{g}}(\mathbf{z}_{\mathrm{g}}; \boldsymbol{\theta}_{\mathrm{g}}), \quad (3)$$

$$\mathbf{m}_{\mathrm{p}} = \boldsymbol{\mathcal{N}}_{\mathrm{p}}(\mathbf{z}_{\mathrm{p}}; \boldsymbol{\theta}_{\mathrm{p}}), \quad (4)$$

where $\mathbf{z}$ represents the input latent vectors of the neural networks that are sampled from standard Gaussian distribution and are non-trainable, and $\boldsymbol{\theta}$ represents the trainable parameters (network weights) of the neural networks. The goal is to estimate $\boldsymbol{\theta}_{\mathrm{g}}$ and $\boldsymbol{\theta}_{\mathrm{p}}$ instead of $\mathbf{m}_{\mathrm{g}}$ and $\mathbf{m}_{\mathrm{p}}$. Model reparameterization with neural networks provides a convenient way to control the range of model parameters, for example $\mathbf{S}_{\mathrm{CO2}}$ and $\mathbf{S}_{\mathrm{w}}$ within [0, 1], which is helpful for the stability of inversion.

Specifically, $\boldsymbol{\mathcal{N}}_{\mathrm{g}}$ is a BNN that takes a 4-dimensional latent vector $\mathbf{z}_{\mathrm{g}}$ as input and outputs a 4-dimensional vector (whose elements correspond to coordination number, critical porosity, cementation m and saturation exponent n, respectively) after the transformation of three fully-connected layers. As illustrated in Figure 2, BNN is a probabilistic model where unlike standard neural networks the weights $\boldsymbol{\theta}$ are not fixed but follow a distribution $p(\boldsymbol{\theta})$ (Dürr et al., 2020) and thus it allows quantifying the uncertainty of the global parameters. The goal of BNN is to find

the posterior distribution $p(\boldsymbol{\theta}|\mathcal{D})$ that best fit the data $\mathcal{D}$. The distribution of network weights allows us to quantify the prediction uncertainty. The solution for the posterior distribution $p(\boldsymbol{\theta}|\mathcal{D})$ is usually not tractable analytically due to the complexity of BNN. We therefore approximate the posterior distribution with a variational distribution $q_\lambda(\boldsymbol{\theta})$ with variational parameters λ according to the variational inference approach. In practice, the variational distribution is generally assumed to be a Gaussian distribution with parameters $\lambda = (\mu, \sigma)$, i.e., mean μ and variance σ. The objective of variational inference is to estimate the variational parameters λ so that $q_\lambda(\boldsymbol{\theta})$ accurately approximates $p(\boldsymbol{\theta}|\mathcal{D})$. Mathematically, this objective is achieved by minimizing the Kullback-Leibler (KL) divergence (Kullback and Leibler, 1951) between the variational and true distribution

$$\mathrm{KL}[q_\lambda(\boldsymbol{\theta})||p(\boldsymbol{\theta}|\mathcal{D})] = \int q_\lambda(\boldsymbol{\theta}) \log \frac{q_\lambda(\boldsymbol{\theta})}{p(\boldsymbol{\theta}|\mathcal{D})} d\boldsymbol{\theta}. \quad (5)$$

Therefore, the corresponding optimization problem associated to BNNs is expressed as determining the optimal variational parameters λ^* as

$$\lambda^* = \underset{\lambda}{\operatorname{argmin}}\{\mathrm{KL}[q_\lambda(\boldsymbol{\theta})||p(\boldsymbol{\theta}|\mathcal{D})] - \mathbb{E}_{\boldsymbol{\theta}\sim q_\lambda}[\log p(\mathcal{D}|\boldsymbol{\theta})]\}, \quad (6)$$

where the first term is the KL divergence and the second (negative) term is the average negative log-likelihood that measures the data misfit.

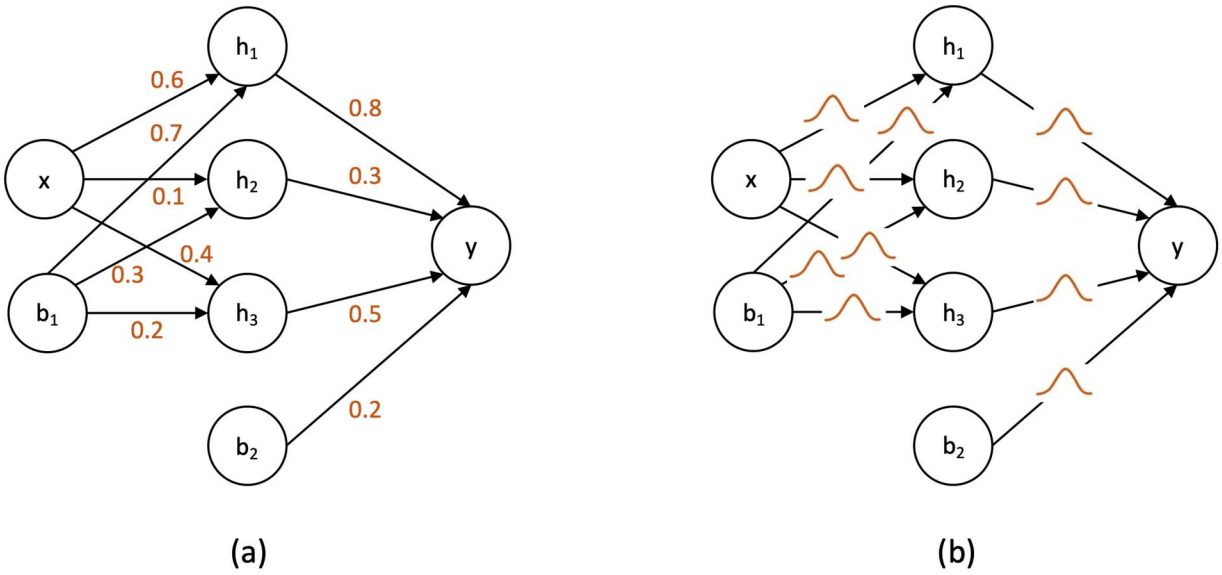

197

198 **Figure 2.** (a) Standard neural network; (b) Bayesian neural network.

199

200 The network $\mathcal{N}_{\mathrm{p}}$ is a CNN that takes another latent vector $\mathbf{z}_{\mathrm{p}}$ of size $n_c \times n_x \times n_y \times n_t$ as
201 input and outputs a $(N_\tau + 1) \times N_x \times N_y \times N_t$ (N_τ is the number of monitoring years, N_x, N_y and
202 N_t are the number of grids along the *x*-, *y*- and *z*- direction) tensor whose elements correspond to
203 the porosity and CO_2 saturations of N_τ years. In the above, N_τ is the number of monitoring
204 surveys, N_x, N_y and N_t are the number of grids along the *x*-, *y*- and *z*- direction, and the output
205 has a dimension of $(N_\tau + 1)$ as there are N_τ surveys and one porosity model that is assumed to
206 be constant over the time of the surveys. In this study, the latent vector is increased by eight
207 times after three up-sampling layers (i.e., $N_x = 8n_x$, $N_y = 8n_y$, $N_t = 8n_t$), while n_c is the
208 number of channels in the CNN input layer. The parameters of CNN are listed in Table 1.

209 **Table 1.** Parameters of each layer in the CNN model.

Layer	Kernel/Scale Factor	Activation function	Output size
1. Input	-	-	64×15×15×28

2.	Conv3D	3×3×3	ReLU	64×15×15×28
3.	Upsample	2	-	64×30×30×56
4.	Conv3D	3×3×3	ReLU	32×30×30×56
5.	Upsample	2	-	32×60×60×112
6.	Conv3D	3×3×3	ReLU	16×60×60×112
7.	Upsample	2	-	16×120×120×224
8.	Conv3D	3×3×3	Sigmoid	4×120×120×224

2.3 Loss Function

The definition of an appropriate objective function (or cost function) is crucial for large-scale geophysical inverse problems. In this study, the objective function is defined as follows

$$J_{\text{loss}}(\boldsymbol{\theta}_{\text{g}}, \boldsymbol{\theta}_{\text{p}}) = \alpha_1 \frac{1}{N_{\text{seis}}} \left\| \mathbf{d}_{\text{seis}} - \tilde{\mathbf{d}}_{\text{seis}} \right\|_2^2 + \alpha_2 \frac{1}{N_{\text{res}}} \left\| \mathbf{d}_{\text{res}} - \tilde{\mathbf{d}}_{\text{res}} \right\|_2^2 + \alpha_3 \text{KL}\left[q(\boldsymbol{\theta}_{\text{g}}) || p(\boldsymbol{\theta}_{\text{g}}) \right] + \alpha_4 \frac{1}{N_{\text{CO2}}} \mathbf{S}_{\text{CO2}}{}^T (1 - \mathbf{S}_{\text{CO2}}), \quad (7)$$

where N_{seis}, N_{res} and N_{CO2} are the number of elements of the seismic data, resistivity data and CO_2 saturation model, respectively; α_i $(i = 1, \dots 4)$ are the weights of the loss terms. The first two terms in Equation 7 are mean square errors (MSE) that measure the mismatch between "true" and predicted data. The third term is the KL divergence of the Bayesian neural network $\boldsymbol{\mathcal{N}}_{\text{g}}(\mathbf{z}_{\text{g}}; \boldsymbol{\theta}_{\text{g}})$ that measures the difference between the variational distribution $q(\boldsymbol{\theta}_{\text{g}})$ and the true distribution $p(\boldsymbol{\theta}_{\text{g}})$ of the BNN weights. The last term is a regularization term to constrain the model values of CO_2 saturation in the interval [0,1] that is necessary for multimodal variables like saturations (Vo and Durlofsky, 2014).

2.4 Differentiable Programming

The inversion workflow is implemented according to the differentiable programming framework. Differentiable programming provides an efficient way to jointly estimate model parameters (i.e., global parameters, spatial distribution of porosity, and time-dependent spatial distribution of CO_2 saturation) where all variables are simultaneously updated.

Differentiable programming organizes a program as a Data Flow Graph (DFG). The DFG is a directed acyclic graph in which graph nodes represent mathematical operations (e.g., addition and multiplication) or variables (tensors) and edges correspond to the flow of intermediate values between the nodes (Martin and Estrin, 1967). Figure 1b shows the DFG of the inversion model in this study. Different from traditional programming paradigms that specify explicit instructions to the computer, constructing DFG is like building blocks in which the program is defined by the input-output data and the associated transformations composed of differentiable blocks. The mechanism of DFG makes the program very flexible and scalable to modify and incorporate prior knowledge.

The network parameters $\boldsymbol{\theta}_{\mathrm{g}}$ and $\boldsymbol{\theta}_{\mathrm{p}}$ in the DFG are learned from the data by minimizing the loss function in Equation 7

$$\left[\widetilde{\boldsymbol{\theta}}_{\mathrm{g}}, \widetilde{\boldsymbol{\theta}}_{\mathrm{p}}\right] = \arg\min_{\boldsymbol{\theta}_{\mathrm{g}}, \boldsymbol{\theta}_{\mathrm{p}}} J_{\mathrm{loss}}\left(\boldsymbol{\theta}_{\mathrm{g}}, \boldsymbol{\theta}_{\mathrm{p}}\right). \quad (8)$$

With the technique of automatic differentiation (Rall, 1981), the gradients of the loss function with respect to $\boldsymbol{\theta}_{\mathrm{g}}$ and $\boldsymbol{\theta}_{\mathrm{p}}$ are automatically computed according to the chain rule

$$\frac{\partial J_{\mathrm{loss}}}{\partial \boldsymbol{\theta}_{\mathrm{p}}} = \left(\frac{\partial J_{\mathrm{loss}}}{\partial \mathbf{f}_{\mathrm{seis}}} \frac{\partial \mathbf{f}_{\mathrm{seis}}}{\partial \mathbf{f}_{\mathrm{rpm}}} \frac{\partial \mathbf{f}_{\mathrm{rpm}}}{\partial \boldsymbol{\mathcal{N}}_{\mathrm{p}}} + \frac{\partial J_{\mathrm{loss}}}{\partial \mathbf{f}_{\mathrm{res}}} \frac{\partial \mathbf{f}_{\mathrm{res}}}{\partial \boldsymbol{\mathcal{N}}_{\mathrm{p}}}\right) \frac{\partial \boldsymbol{\mathcal{N}}_{\mathrm{p}}}{\partial \boldsymbol{\theta}_{\mathrm{p}}}, \quad (9)$$

$$\frac{\partial J_{\mathrm{loss}}}{\partial \boldsymbol{\theta}_{\mathrm{g}}} = \frac{\partial J_{\mathrm{loss}}}{\partial \mathbf{f}_{\mathrm{seis}}} \frac{\partial \mathbf{f}_{\mathrm{seis}}}{\partial \mathbf{f}_{\mathrm{rpm}}} \frac{\partial \mathbf{f}_{\mathrm{rpm}}}{\partial \boldsymbol{\mathcal{N}}_{\mathrm{g}}} \frac{\partial \boldsymbol{\mathcal{N}}_{\mathrm{g}}}{\partial \boldsymbol{\theta}_{\mathrm{g}}} + \frac{\partial J_{\mathrm{loss}}}{\partial \mathbf{f}_{\mathrm{res}}} \frac{\partial \mathbf{f}_{\mathrm{res}}}{\partial \boldsymbol{\mathcal{N}}_{\mathrm{g}}} \frac{\partial \boldsymbol{\mathcal{N}}_{\mathrm{g}}}{\partial \boldsymbol{\theta}_{\mathrm{g}}}. \quad (10)$$

The optimal network parameters $\widetilde{\boldsymbol{\theta}}_{\mathrm{g}}$ and $\widetilde{\boldsymbol{\theta}}_{\mathrm{p}}$ are then obtained by the gradient-based

247 backpropagation method. Here, we use the adaptive moment estimation algorithm (Adam)
248 (Kingma and Ba, 2014), which is computationally efficient for high-dimensional problems.
249

250 ## 3. Application

251 We demonstrate the proposed model for joint geophysical monitoring of CO_2 storage with an
252 synthetic model and data modified from the Sleipner 2019 Benchmark Model
253 (https://co2datashare.org/dataset/sleipner-2019-benchmark-model). The Sleipner field located in
254 the Norwegian Sea is the first commercial GCS plant and is the longest ongoing CO_2 storage
255 project in the world. The Utsira Formation is the target storage unit, consisting of nine sandstone
256 layers that are vertically separated by eight thin shale layers with low-permeability and a caprock
257 layer. Porosity and permeability of each layer are assumed to be constant in the original
258 benchmark dataset. To make the GCS model more realistic, porosity and permeability of each
259 layer of the reservoir model used in this study are taken to be spatially variable and are
260 geostatistically simulated by sequential Gaussian simulation (SGS) (Deutsch and Journel, 1998)
261 to mimic the spatial heterogeneity of subsurface rocks. Porosity and permeability are assumed to
262 be constant in time. The reference "true" models of porosity and permeability are shown in
263 Figure 3a and 3b, respectively. The GCS model consists of 64×118×263 grid cells. The lateral
264 resolution of the model is 50 m by 50 m and the vertical resolution is about 2 m for the sandstone
265 layers, 0.5 m for the shale layers and 5 m for the caprock. The model parameters such as fluid
266 properties and well configurations are provided in the benchmark dataset. The multiphase flow
267 behavior of CO_2 flow is simulated from the year 1996 to 2010 using the Open Porous Media
268 Flow reservoir simulator (Rasmussen et al., 2021). The detailed parameters of the reservoir are
269 listed in Table 2.

Table 2. Reservoir model parameters of the example modified from the Sleipner benchmark model.

Layer	Formation	Porosity mean	Porosity range	Permeability mean (mD)	Permeability range (mD)
1	Caprock	0.016	[0.002, 0.036]	5.93e-4	[0, 0.0058]
2	Sandstone	0.17	[0.018, 0.40]	734.44	[0.031, 11969]
3	Shale	0.017	[0.002, 0.04]	7.36e-4	[0, 0.0115]
4	Sandstone	0.18	[0.018, 0.35]	629.81	[0.028, 5172.8]
5	Shale	0.017	[0.002, 0.036]	5.55e-4	[0, 0.0059]
6	Sandstone	0.17	[0.021, 0.35]	559.58	[0.048, 5317.1]
7	Shale	0.018	[0.002, 0.033]	6.40e-4	[0, 0.0041]
8	Sandstone	0.20	[0.027, 0.35]	810.07	[0.12, 5439.1]
9	Shale	0.022	[0.003, 0.034]	0.0010	[0, 0.0048]
10	Sandstone	0.21	[0.024, 0.38]	1065.6	[0.079, 9202.0]
11	Shale	0.021	[0.003, 0.039]	9.75e-4	[0, 0.0097]
12	Sandstone	0.20	[0.019, 0.39]	822.73	[0.037, 9599.8]
13	Shale	0.019	[0.002, 0.037]	7.87e-4	[0, 0.0078]
14	Sandstone	0.20	[0.02, 0.40]	910.26	[0.043, 11269]
15	Shale	0.019	[0.003, 0.036]	8.93e-4	[0, 0.0067]
16	Sandstone	0.19	[0.019, 0.35]	771.31	[0.033, 5152.0]
17	Shale	0.018	[0.003, 0.032]	6.68e-4	[0, 0.0035]
18	Sandstone	0.18	[0.019, 0.35]	701.91	[0.035, 5604.5]

In this application, we aim to quantify porosity and CO_2 plumes at years 2000, 2003 and 2006 from the base seismic and resistivity surveys at year 1996 (before CO_2 injection) and monitor seismic and resistivity surveys of the three years. The area of interest is a sub-region of the reservoir model around the injector well (dashed red rectangle in Figure 4a). The synthetic data in the area of interest are simulated in time domain and consist of 120×120×224 grid cells with lateral resolution of 25 m (downscaled by scatter interpolation in 3-D) and time interval of 1

ms. Porosity and CO_2 saturations in the area of interest are shown in Figure 3c – f. The reference "true" seismic and resistivity responses predicted by the forward model (Section 2.1) at year 1996, 2000, 2003 and 2006 are shown in Figure 4 – 7. Observations of year 1996 are base surveys that are acquired before CO_2 injection, while observations of the latter three years are monitor surveys aiming to characterize CO_2 displacement. The pre-stack seismic data include near, mid and far stacks corresponding to incidence angles of 12, 24 and 36 degrees, respectively. The dominant frequencies of wavelets for near, mid and far stacks are 30, 25 and 20 Hz, respectively. We introduce measurement error to the seismic data by adding Gaussian noise with zero mean and 0.02 standard deviation to the reflection coefficients and then convolve them with wavelets. For the resistivity, we add Gaussian noise with zero mean and 0.5 standard deviation in the common logarithm scale and then smooth it with a Gaussian filter with standard deviation of 3 pixels. This represents for example, resistivity that would be available from an inversion of CSEM data. The implementation details and the parameters of the reference models and geophysical observations are included in the code.

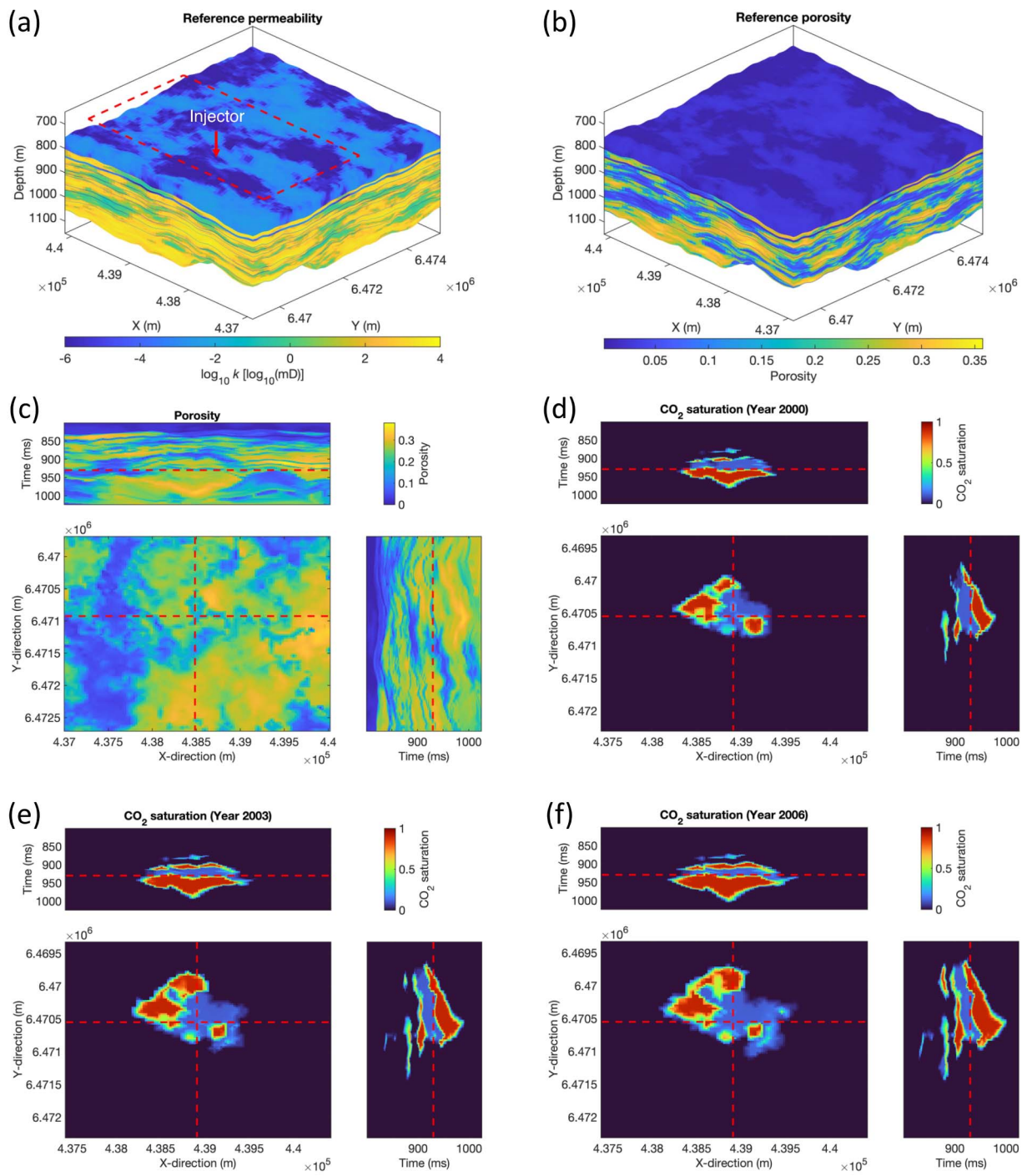

292

293 **Figure 3.** Reservoir models of porosity (a) (dashed red rectangle is the area of interest) and permeability

294 (b) for CO_2 flow simulation. Porosity (c) and CO_2 saturations at year 2000 (d), 2003 (e) and 2006 (f) in

295 the area of interest. The injector well is located at the intersection of the dashed red lines.

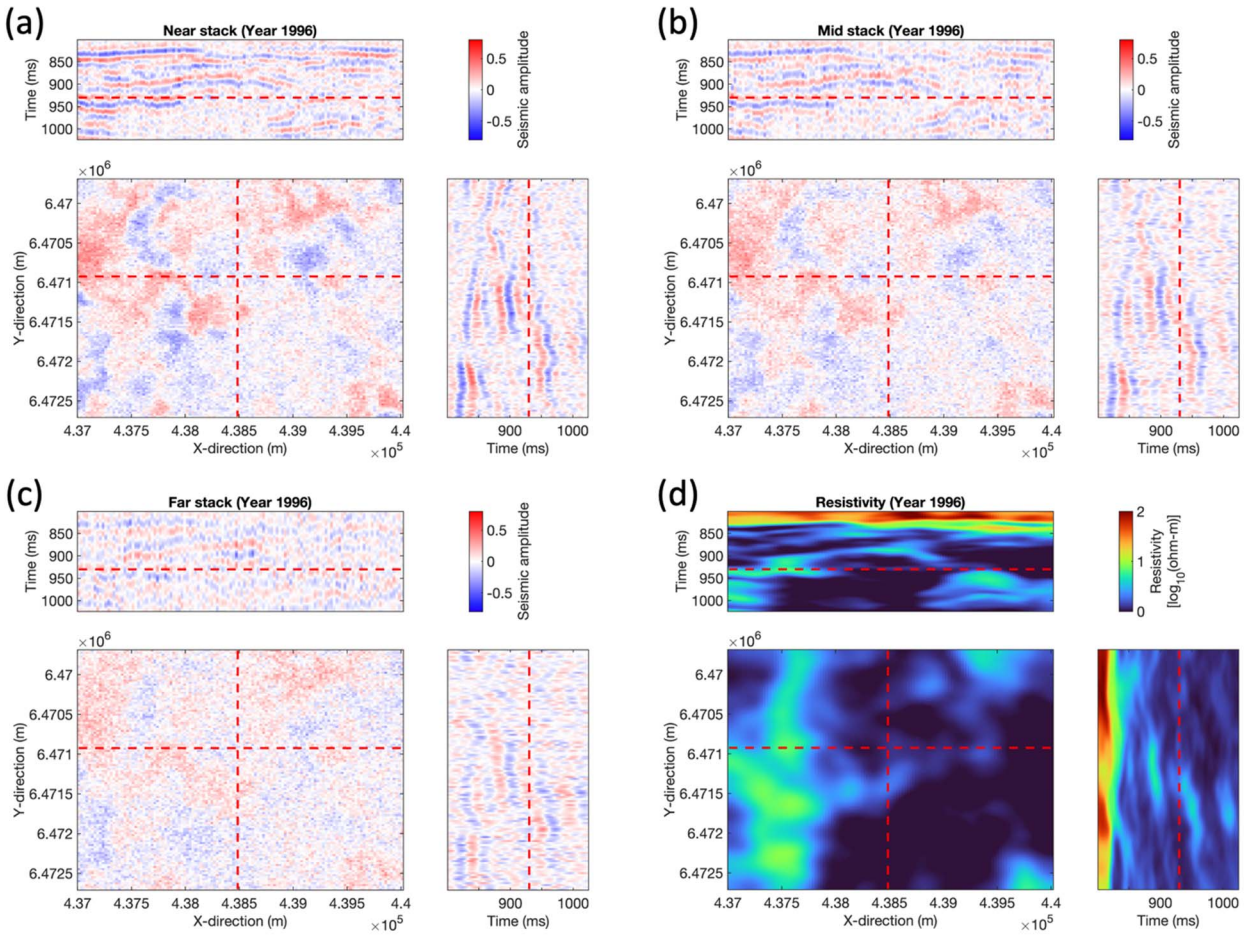

Figure 4. Observations of year 1996 (base survey): (a) near seismic stack; (b) mid seismic stack; (c) far seismic stack; (d) resistivity data.

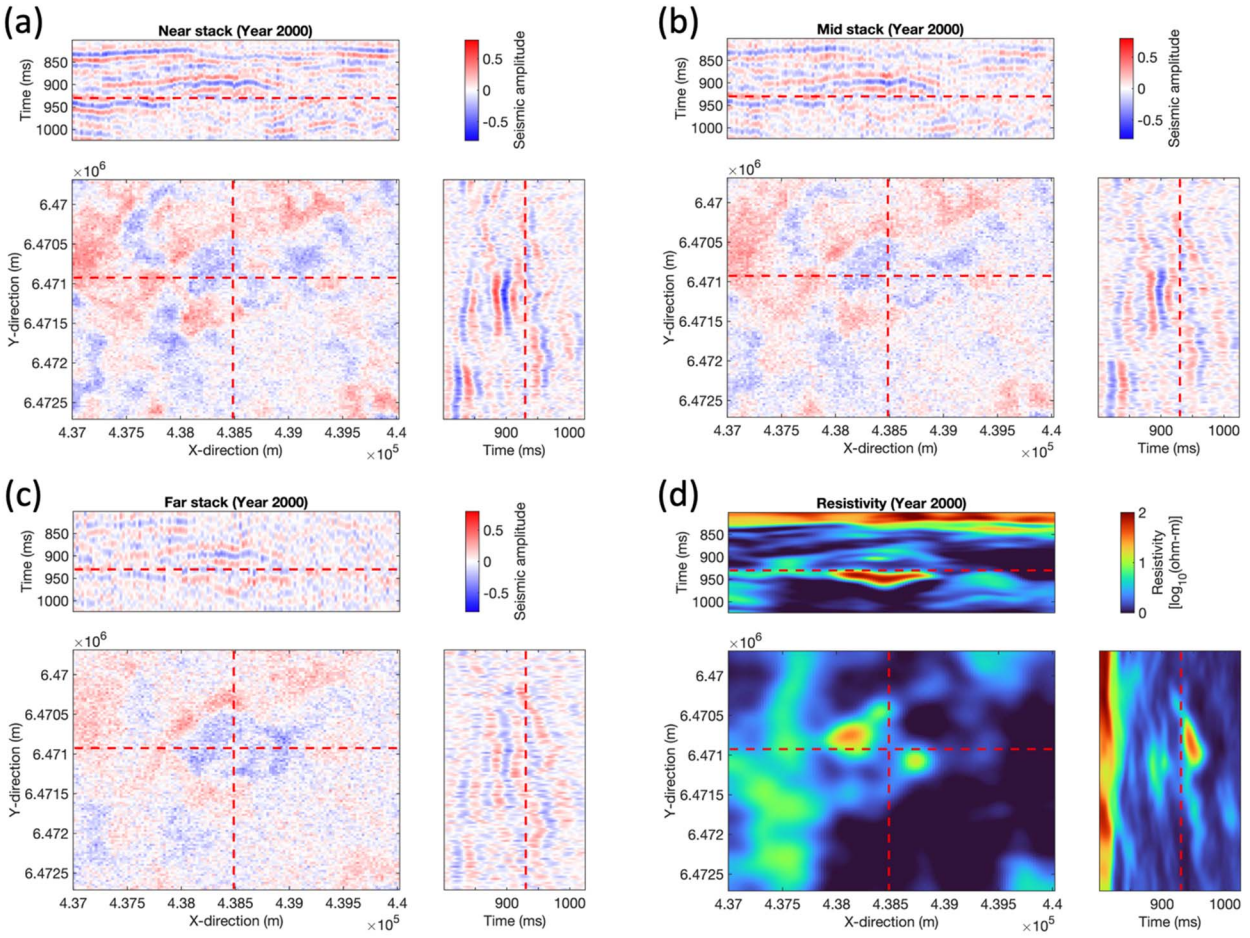

299

300 **Figure 5.** Observations of year 2000 (monitor survey): (a) near seismic stack; (b) mid seismic stack; (c)

301 far seismic stack; (d) resistivity data.

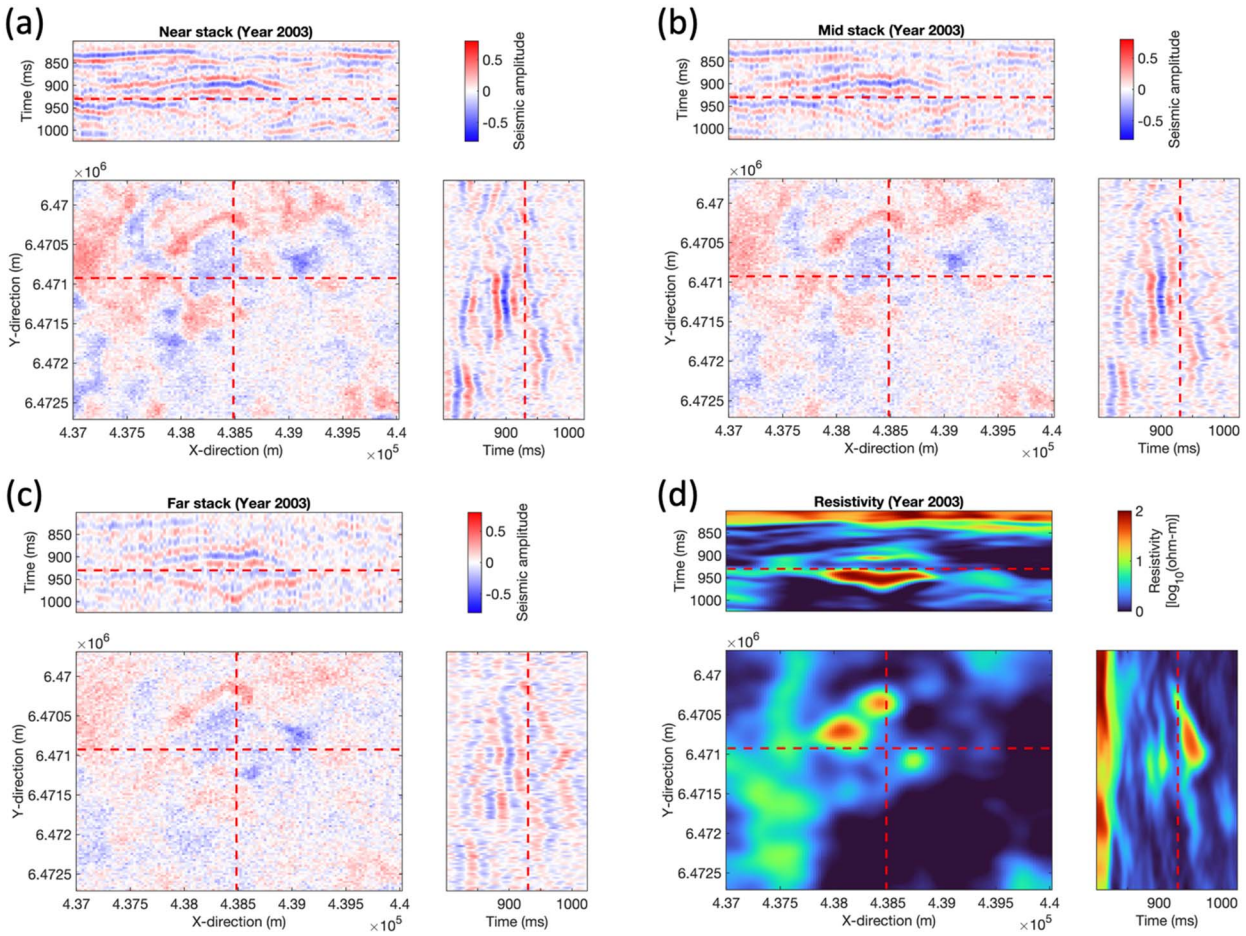

Figure 6. Observations of year 2003 (monitor survey): (a) near seismic stack; (b) mid seismic stack; (c) far seismic stack; (d) resistivity data.

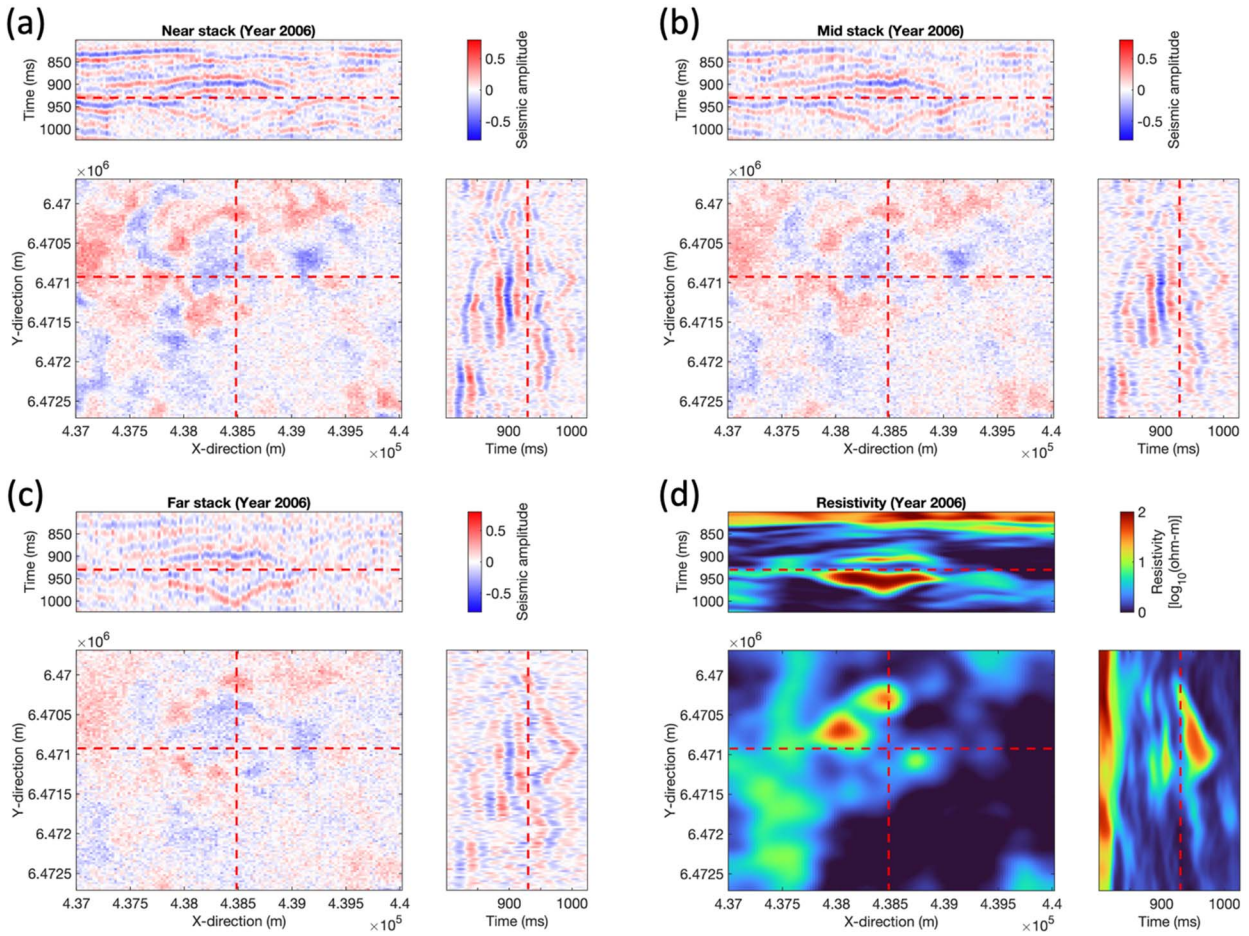

Figure 7. Observations of year 2006 (monitor survey): (a) near seismic stack; (b) mid seismic stack; (c) far seismic stack; (d) resistivity data.

Figure 8 shows the seismic and resistivity responses as function of the change in CO_2 saturation and the sensitivity of P-impedance and resistivity to CO_2 saturation. In this case, it will be hard to detect CO_2 saturation changes above 0.3 using time-lapse seismic data. Inversion of seismic data alone can predict the porosity model and roughly delineate the CO_2 plumes, but the CO_2 saturations are obviously underestimated. Instead, time-lapse resistivity data are highly sensitive to changes in fluid volumes but the spatial resolution of the resistivity measurements is limited and the coupling of porosity and the CO_2 saturation in Equation 2 makes the inversion of

316 resistivity data by itself highly uncertain. The inverted results using only one type of data, i.e.,

317 seismic or resistivity data alone, are shown in Figure 9 and 10.

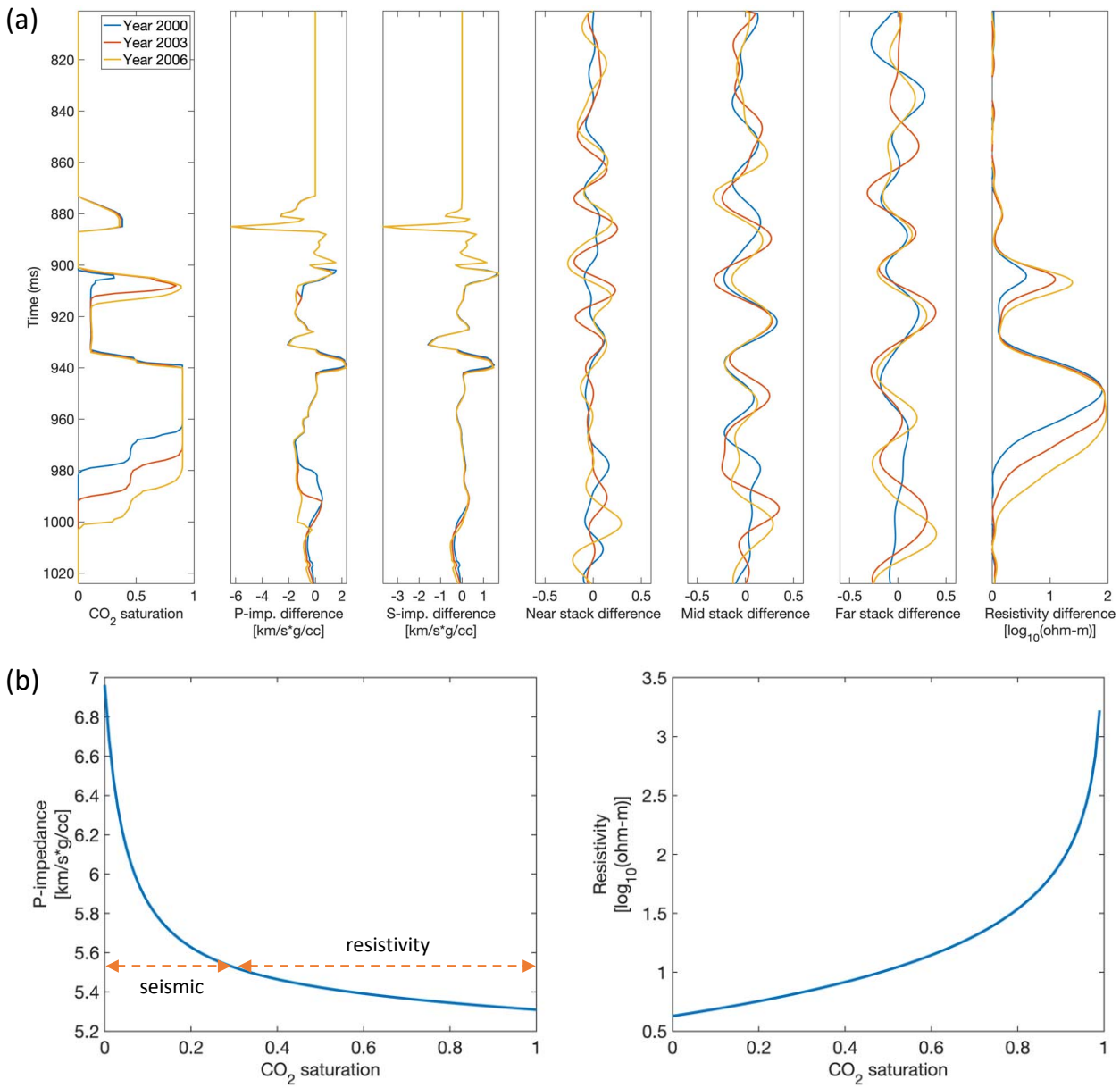

318

319 **Figure 8.** (a) Geophysical responses to the change in CO_2 saturation and (b) sensitivity of P-impedance

320 and resistivity to CO_2 saturation.

321

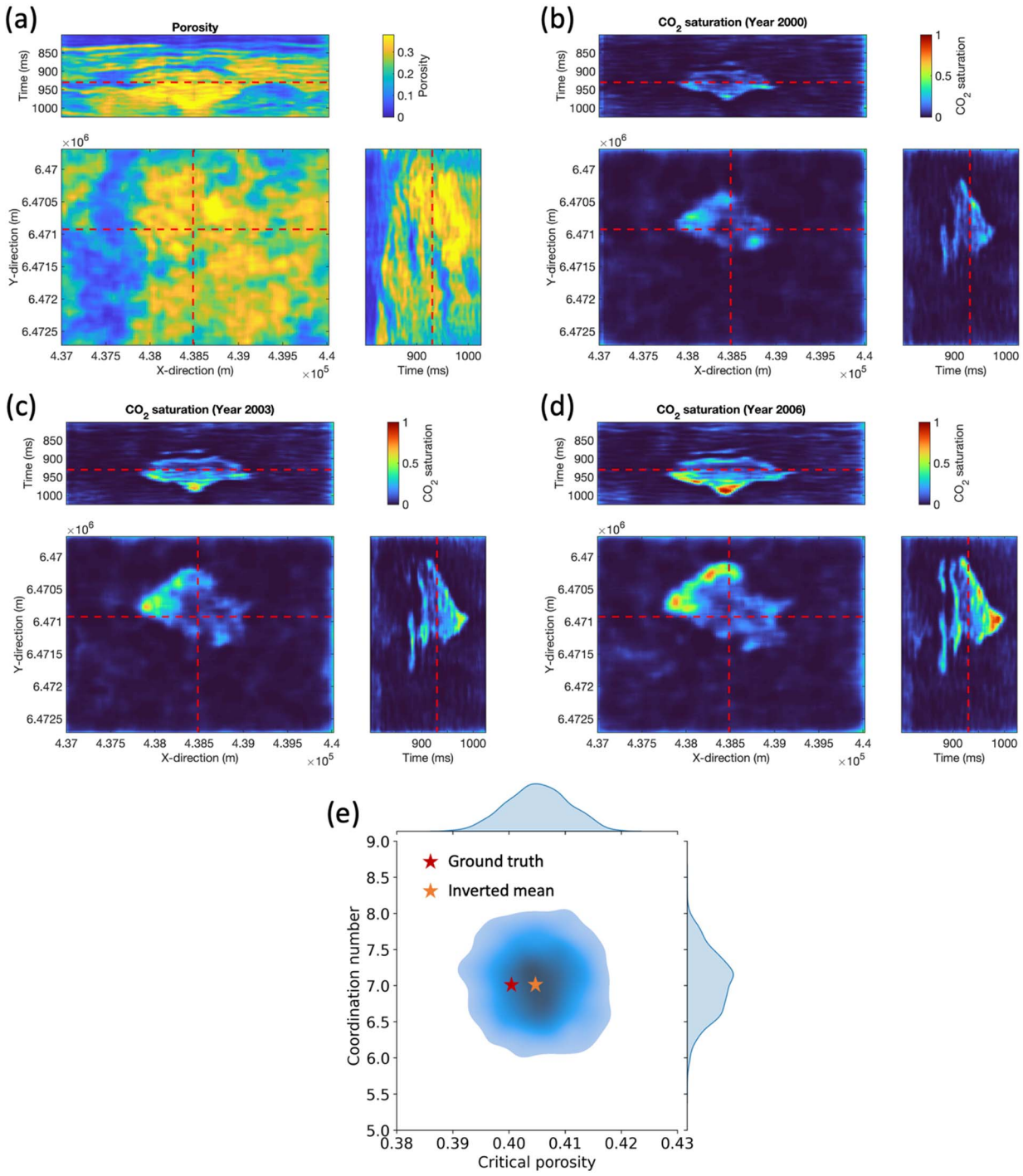

Figure 9. Inverted results with only seismic data: (a) porosity; (b) CO_2 saturation at year 2000; (c) CO_2 saturation at year 2003; (d) CO_2 saturation at year 2006; (e) critical porosity and coordination number obtained from the trained BNN.

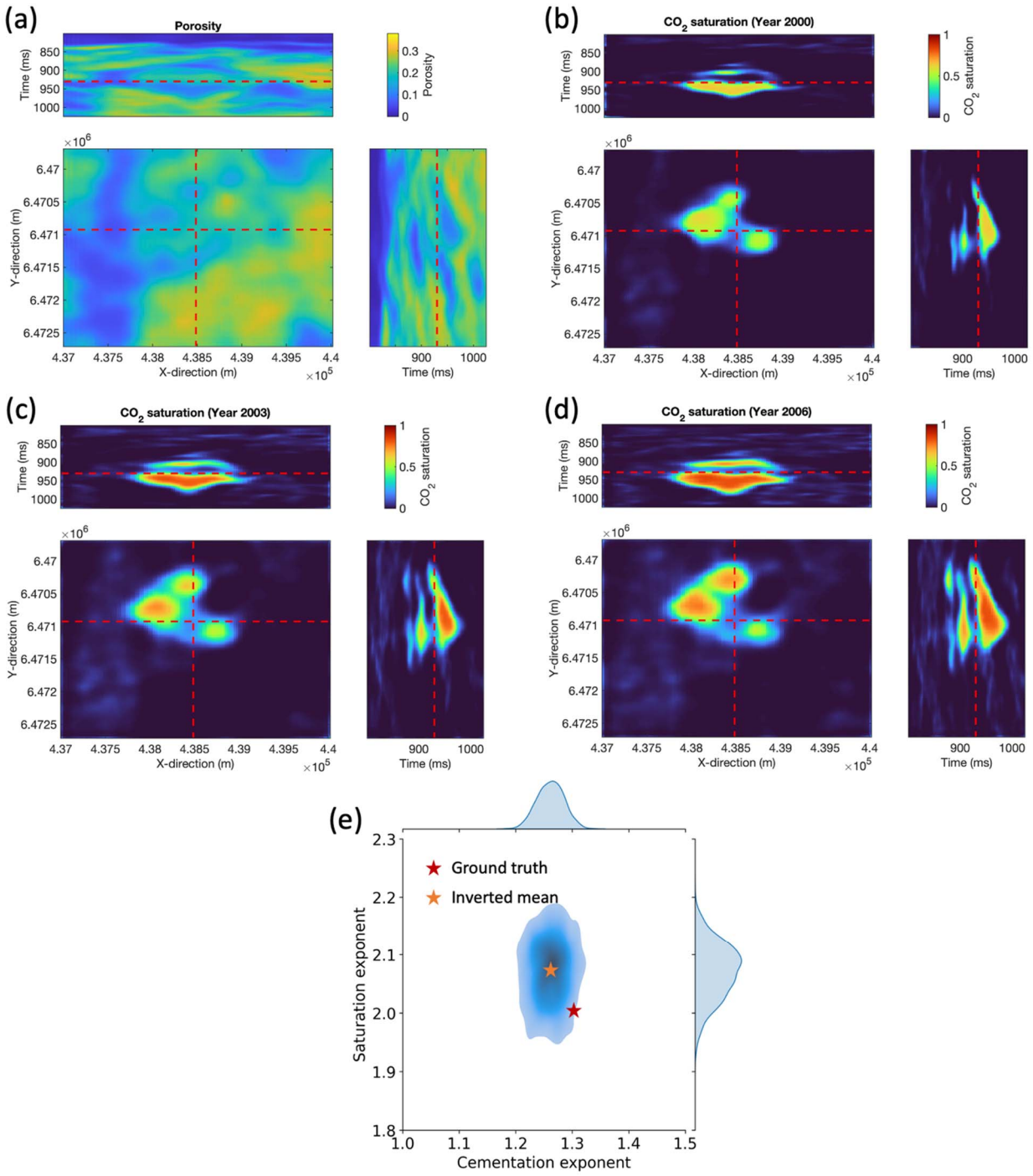

326

327 **Figure 10.** Inverted results with only resistivity data: (a) porosity; (b) CO_2 saturation at year 2000; (c)

328 CO_2 saturation at year 2003; (d) CO_2 saturation at year 2006; (e) cementation and saturation exponents

329 obtained from the trained BNN.

330

The proposed differentiable physics model provides an efficient way to jointly invert time-lapse seismic and resistivity data for the simultaneous prediction of porosity and CO_2 saturations. Figure 11a – d shows the inverted models of porosity and CO_2 saturations at years 2000, 2003 and 2006. Compared to the reference models in Figure 3, the predicted porosity and CO_2 saturations accurately match the true model. The R^2 score of porosity is 0.92 and of CO_2 saturations are 0.90, 0.92 and 0.92 for the three years under examination. Figure 11e and 11f show the global model parameters, i.e., critical porosity, coordination number, cementation and saturation exponent, with associated uncertainties predicted by the BNN. The mean values of the predicted global parameters are close to the true parameters used to generate the synthetic data. Unlike traditional trace-by-trace inversion algorithms, the proposed model predicts geologically consistent and spatially continuous models, thanks to the simultaneous inversion in 4-D and the prior information encoded in the CNN for model re-parameterization (Zhu et al., 2022). The total loss defined by Equation 7 and the MSE between the predicted and true data over iterations are shown in Figure 12. The other advantage of the proposed method is the computational efficiency. The inversion takes approximately 2.2 hours with an Intel Xeon E5-1650 CPU and the computing time is further reduced to 15 minutes with a Nvidia GTX 1080 GPU. Overall, the proposed inversion model shows great promises for joint geophysical monitoring for CO_2 storage and could be applied to any large scale geophysical inverse problem with noisy data from multiple sources.

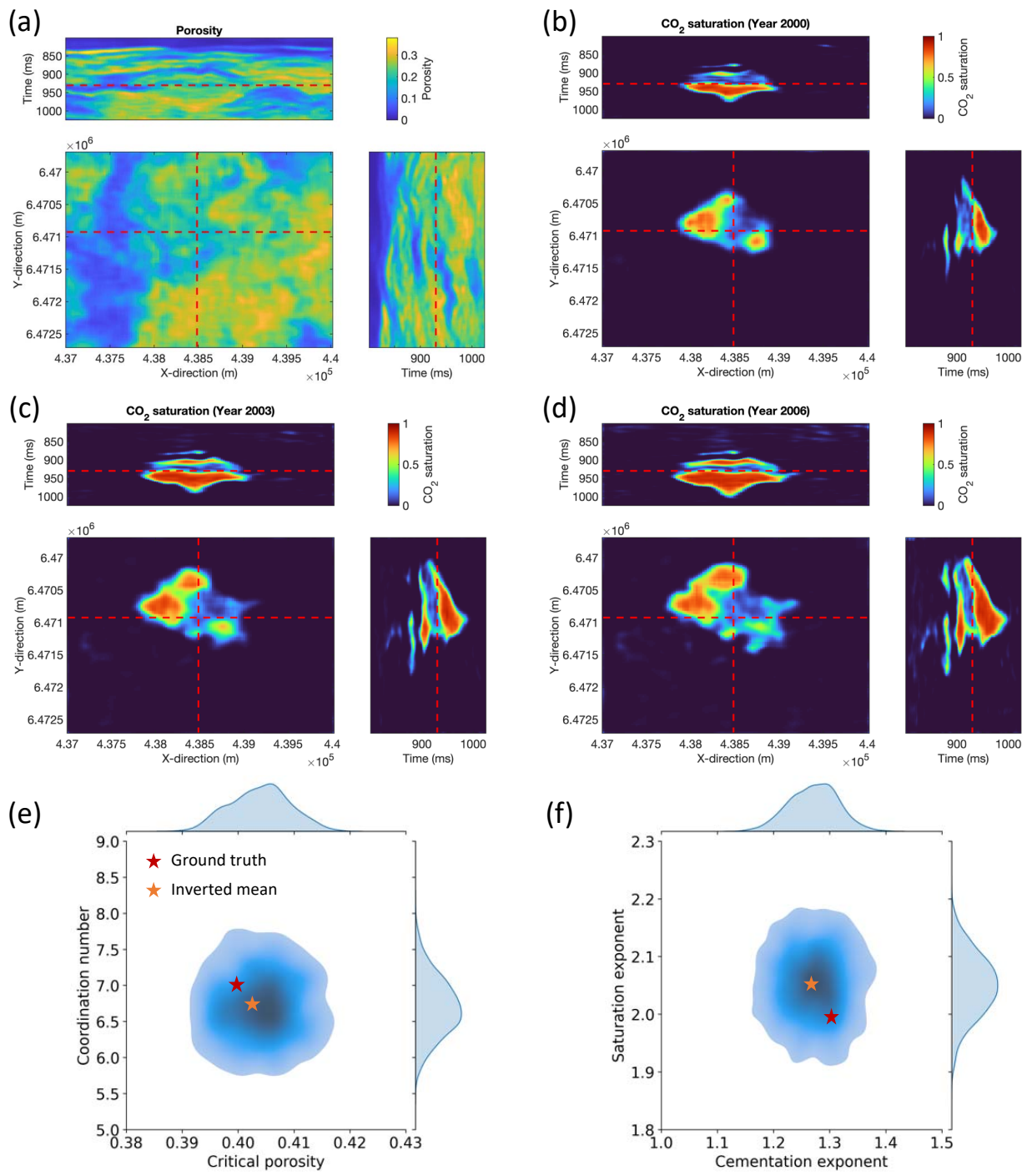

Figure 11. Joint inversion results of the proposed model: (a) porosity; (b) CO_2 saturation at year 2000; (c) CO_2 saturation at year 2003; (d) CO_2 saturation at year 2006; (e) posterior distribution of critical porosity and coordination number; and (f) cementation and saturation exponents, obtained from the trained BNN.

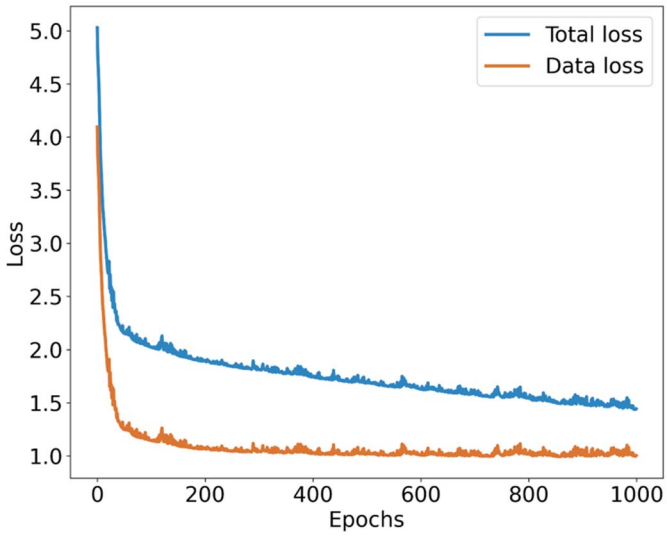

Figure 12. Loss function values over iterations.

4. Discussion

The differentiable physics model provides a promising tool for joint inversion of large geophysical data for GCS monitoring. The synthetic example focuses on the inversion of pre-stack seismic and resistivity data based on the seismic wave propagation and elastic-electrical rock physics models and provides an accurate validation of the approach. The proposed model can be also extended to the inversion and assimilation of other data types and other geophysical operators, including, for example, seismic angle gathers with full waveform inversion or amplitude and phase measurements of electromagnetic fields with electromagnetic wave propagation models by implementing the forward operators according to the differentiable programming approach. According to the proposed model, the gradients of the forward operators can be efficiently evaluated by automatic differentiation and the computational effort can be deployed to high-performance computing platforms (e.g., GPUs). One potential limitation of the proposed model is the high demand for computing resources in cases with extremely large

372 geological models and geophysical data (up to billions of grids), especially when involving
373 computationally intensive forward modeling. A possible solution might include the integration of
374 PINNs and deep-learning surrogate models into the inversion model.
375
376 **5. Conclusion**

377 A novel inversion model has been developed for the joint inversion of large-scale
378 geophysical data from different sources and applied to geologic carbon sequestration monitoring.
379 The proposed model is built upon the technique of differentiable physics with the integration of
380 deep neural networks for model re-parameterization. Thanks to automatic differentiation and
381 parallel computing, the inversion is computationally efficient, and all parameters are updated
382 simultaneously to minimize the loss function through the backpropagation algorithm. Moreover,
383 the model can also predict global model parameters that are uncertain in the forward model. The
384 presented approach has been validated on a synthetic example modified from the Sleipner
385 benchmark model. The inverted models accurately reproduced the actual reference model,
386 including porosity and time dependent CO_2 saturation. We conclude that the proposed model
387 provides an efficient and accurate tool to assimilate multiphysics data for subsurface monitoring.
388

389 **Appendix A: Unconsolidated sand model**

390 In the unconsolidated sand model (Dvorkin and Nur 1996), the matrix bulk and shear moduli
391 (K_{mat} and μ_{mat}) are computed by the Voigt-Reuss-Hill average as function of the mineral
392 fractions (e.g., clay and quartz volumes), while the moduli of dry rock (K_{HM} and μ_{HM}) at the
393 critical porosity ϕ_0 are computed using the Hertz-Mindlin equations (Mindlin, 1949)

$$K_{\mathrm{HM}} = \sqrt[3]{\frac{P_e[n(1-\phi_0)\mu_{\mathrm{mat}}]^2}{18[\pi(1-\nu)]^2}}, \tag{A-1}$$

$$\mu_{\mathrm{HM}} = \frac{5-4\nu}{5(2-\nu)}\sqrt[3]{\frac{3P_e[n(1-\phi_0)\mu_{\mathrm{mat}}]^2}{2[\pi(1-\nu)]^2}}, \tag{A-2}$$

where P_e is the effective pressure, ν is the grain Poisson's ratio and n is the coordination number (i.e., average number of contacts per grain). Then, the moduli of the dry rock (K_{dry} and μ_{dry}) with porosity in the range $[0, \phi_0]$ are obtained by interpolating two end members (matrix and dry rock moduli at critical porosity) using the modified Hashin-Shtrikman lower bounds (Hashin and Shtrikman 1963)

$$K_{\mathrm{dry}} = \left(\frac{\frac{\phi}{\phi_0}}{K_{\mathrm{HM}}+\frac{4}{3}\mu_{\mathrm{HM}}} + \frac{1-\frac{\phi}{\phi_0}}{K_{\mathrm{mat}}+\frac{4}{3}\mu_{\mathrm{HM}}}\right)^{-1} - \frac{4}{3}\mu_{\mathrm{HM}}, \tag{A-3}$$

$$\mu_{\mathrm{dry}} = \left(\frac{\frac{\phi}{\phi_0}}{\mu_{\mathrm{HM}}+\frac{1}{6}\xi\mu_{\mathrm{HM}}} + \frac{1-\frac{\phi}{\phi_0}}{\mu_{\mathrm{mat}}+\frac{1}{6}\xi\mu_{\mathrm{HM}}}\right)^{-1} - \frac{1}{6}\xi\mu_{\mathrm{HM}}, \tag{A-4}$$

with

$$\xi = \frac{9K_{\mathrm{HM}}+8\mu_{\mathrm{HM}}}{K_{\mathrm{HM}}+2\mu_{\mathrm{HM}}}. \tag{A-5}$$

For the fluid saturated rock, the bulk and shear moduli (K_{sat} and μ_{sat}) are computed using fluid substitution with Gassmann's equations (Gassmann 1951)

$$K_{\mathrm{sat}} = K_{\mathrm{dry}} + \frac{\left(1-\frac{K_{\mathrm{dry}}}{K_{\mathrm{mat}}}\right)^2}{\frac{\phi}{K_{\mathrm{fl}}}+\frac{1-\phi}{K_{\mathrm{mat}}}-\frac{K_{\mathrm{dry}}}{K_{\mathrm{mat}}^2}}, \tag{A-6}$$

$$\mu_{\mathrm{sat}} = \mu_{\mathrm{dry}}. \tag{A-7}$$

where K_{fl} is the bulk modulus of the fluid phase and it depends on the water and CO_2 saturations and their corresponding bulk moduli. Here the bulk moduli of brine water and CO_2 are 3.06 and 0.10 GPa, respectively; the density of brine water and CO_2 are 1.08 and 0.72 g/cc, respectively (Davis et al., 2019). Finally, the P- and S-wave velocities can be computed from the moduli by

definition

$$V_p = \sqrt{\frac{K_{\mathrm{sat}} + \frac{4}{3}\mu_{\mathrm{sat}}}{\rho_{\mathrm{sat}}}}, \tag{A-8}$$

$$V_s = \sqrt{\frac{\mu_{\mathrm{sat}}}{\rho_{\mathrm{sat}}}}, \tag{A-9}$$

where ρ_{sat} is the density of the saturated rock which is weighted average of the matrix density ρ_{mat} and fluid density ρ_{fl}

$$\rho_{\mathrm{sat}} = (1-\phi)\rho_{\mathrm{mat}} + \phi\rho_{\mathrm{fl}}. \tag{A-10}$$

Appendix B: Convolution-based seismic model

In the convolution-based seismic wave propagation model (Yilmaz, 2001; Grana et al., 2021), the seismic response $\mathbf{d}_{\mathrm{seis}}(x,t,\theta)$ is computed by convolving the source wavelet $\boldsymbol{w}(\theta)$ with a series of reflectivity coefficients $\boldsymbol{R}(x,t,\theta)$ as

$$\mathbf{d}_{\mathrm{seis}}(x,t,\theta) = \boldsymbol{w}(\theta) * \boldsymbol{R}(x,t,\theta), \tag{B-1}$$

where x is the spatial location, t is the two-way vertical seismic travel time and θ is the angle of incidence. For pre-stack seismic data, the reflectivity coefficients $\boldsymbol{R}(x,t,\theta)$ are obtained from the elastic parameters (P-wave velocity V_P, S-wave velocity V_S, and density ρ) by the Knott-Zoeppritz equations (Aki and Richards, 2002)

$$\begin{bmatrix} R_{PP}(\theta_1) \\ R_{PS}(\theta_1) \\ T_{PP}(\theta_1) \\ T_{PS}(\theta_1) \end{bmatrix} = \begin{bmatrix} -\sin\theta_1 & -\cos\varphi_1 & \sin\theta_2 & \cos\varphi_2 \\ \cos\theta_1 & -\sin\varphi_1 & \cos\theta_2 & -\sin\varphi_2 \\ \sin 2\theta_1 & \frac{V_{P1}}{V_{S1}}\cos 2\varphi_1 & \frac{\rho_2 V_{S2}^2 V_{P1}}{\rho_1 V_{S1}^2 V_{P2}}\sin 2\theta_2 & \frac{\rho_2 V_{S2} V_{P1}}{\rho_1 V_{S1}^2}\cos 2\varphi_2 \\ -\cos 2\phi_1 & \frac{V_{S1}}{V_{P1}}\sin 2\varphi_1 & \frac{\rho_2 V_{P2}}{\rho_1 V_{P1}}\cos 2\phi_2 & -\frac{\rho_2 V_{S2}}{\rho_1 V_{P1}}\sin 2\varphi_2 \end{bmatrix}^{-1} \begin{bmatrix} \sin\theta_1 \\ \cos\theta_1 \\ \sin 2\theta_1 \\ \cos 2\phi_1 \end{bmatrix}, \quad \text{(B-2)}$$

where θ_1 is the angle of incidence, θ_2 is the angle of the transmitted P-wave, φ_1 is the angle of reflected S-wave, and φ_2 is the angle of the transmitted S-wave; $R_{PP}(\theta_1)$, $R_{PS}(\theta_1)$, $T_{PP}(\theta_1)$ and $T_{PS}(\theta_1)$ are the reflected P-, reflected S-, transmitted P-, and transmitted S-wave amplitude coefficients, respectively; the subscripts 1 and 2 represent elastic parameters of the upper and lower layers, respectively. In this study, we only consider reflected P-wave amplitudes (i.e., R_{PP}).

Data Availability Statement

The code and data are freely available on the GitHub repository (https://github.com/theanswer003/JointInvDP) (Liu, 2022).

Acknowledgements

We acknowledge the sponsors of the Stanford Center for Earth Resources Forecasting (SCERF) and support from Prof. Steve Graham, the Dean of the Stanford School of Earth, Energy and Environmental Sciences. The authors also would like to thank Equinor for sharing the Sleipner benchmark model.

References

- Aki, K., & Richards, P. G. (2002). Quantitative Seismology: *University Science Books, 2nd ed*.
- Aminu, M.D., Nabavi, S.A., Rochelle, C.A., & Manovic, V. (2017). A review of developments in carbon dioxide storage. *Applied Energy, 208*, pp.1389-1419.
- Archie, G.E. (1942). The electrical resistivity log as an aid in determining some reservoir characteristics. *Transactions of the AIME, 146*(01), pp.54-62.
- Bhuyian, A.H., Landrø, M., & Johansen, S.E. (2012). 3D CSEM modeling and time-lapse sensitivity analysis for subsurface CO_2 storage. *Geophysics, 77*(5), pp.E343-E355.
- Bonneville, A., Black, A.J., Hare, J.L., Kelley, M.E., Place, M., & Gupta, N. (2021). Time-lapse borehole gravity imaging of CO_2 injection and withdrawal in a closed carbonate reef. *Geophysics, 86*(6), pp.G113-G132.
- Caspari, E., Müller, T.M., & Gurevich, B. (2011). Time-lapse sonic logs reveal patchy CO_2 saturation in-situ. *Geophysical Research Letters, 38*(13).
- Chadwick, A., Williams, G., Delepine, N., Clochard, V., Labat, K., Sturton, S., Buddensiek, M.L., Dillen, M., Nickel, M., Lima, A.L., & Arts, R. (2010). Quantitative analysis of time-lapse seismic monitoring data at the Sleipner CO_2 storage operation. *The Leading Edge, 29*(2), pp.170-177.
- Davis, T.L., Landrø, M., & Wilson, M. (2019). Geophysics and geosequestration. *Cambridge University Press*.
- Deutsch, C.V., & Journal, A.G. (1998). GSLIB: Geostatistical software library and user's guide. *New York: Oxford University Press*.
- Dupuy, B., Romdhane, A., Nordmann, P.L., Eliasson, P., & Park, J. (2021). Bayesian rock-

physics inversion: Application to CO_2 storage monitoring. *Geophysics, 86*(4), pp.M101-M122.

- Dürr, O., Sick, B., & Murina, E. (2020). Probabilistic Deep Learning: With Python, Keras and TensorFlow Probability. *Manning Publications*.
- Dvorkin, J., & Nur, A. (1996). Elasticity of high-porosity sandstones: Theory for two North Sea data sets. *Geophysics, 61*(5), pp.1363-1370.
- Egorov, A., Pevzner, R., Bóna, A., Glubokovskikh, S., Puzyrev, V., Tertyshnikov, K., & Gurevich, B. (2017). Time-lapse full waveform inversion of vertical seismic profile data: Workflow and application to the CO2CRC Otway project. *Geophysical Research Letters, 44*(14), pp.7211-7218.
- Eliasson, P., Romdhane, A., Jordan, M., & Querendez, E. (2014). A synthetic Sleipner study of CO_2 quantification using controlled source electro-magnetics and full waveform inversion. *Energy Procedia, 63*, pp.4249-4263.
- Gasperikova, E., Appriou, D., Bonneville, A., Feng, Z., Huang, L., Gao, K., Yang, X., & Daley, T. (2022). Sensitivity of geophysical techniques for monitoring secondary CO_2 storage plumes. *International Journal of Greenhouse Gas Control, 114*, p.103585.
- Gassmann, F. (1951). Elastic waves through a packing of spheres. *Geophysics 16*(4), 673–685.
- Glubokovskikh, S., Pevzner, R., Gunning, J., Dance, T., Shulakova, V., Popik, D., Popik, S., Bagheri, M., & Gurevich, B. (2020). How well can time-lapse seismic characterize a small CO_2 leakage into a saline aquifer: CO2CRC Otway 2C experiment (Victoria, Australia). *International Journal of Greenhouse Gas Control, 92*, p.102854.
- Grana, D., Mukerji, T., & Doyen, P. (2021). Seismic reservoir modeling: Theory, examples,

and algorithms. *John Wiley & Sons*.

- Grude, S., Landrø, M., & Osdal, B. (2013). Time-lapse pressure–saturation discrimination for CO_2 storage at the Snøhvit field. *International Journal of Greenhouse Gas Control*, 19, pp.369-378.
- Hernández, A., Millerioux, G., & Amigó, J.M. (2022). Differentiable programming: Generalization, characterization and limitations of deep learning. *arXiv preprint* arXiv:2205.06898.
- Hashin, Z., & Shtrikman, S. (1963). A variational approach to the theory of the elastic behaviour of multiphase materials. *Journal of the Mechanics and Physics of Solids, 11*(2), 127–140.
- Huang, L. (2022). Geophysical Monitoring for Geologic Carbon Storage. *Wiley*.
- Kingma, D.P., & Ba, J. (2014). Adam: A method for stochastic optimization. *arXiv preprint* arXiv:1412.6980.
- Kullback, S., & Leibler, R.A. (1951). On information and sufficiency. *Ann Math Stat 22*:79–86.
- Li, B., & Li, Y.E. (2021). Neural Network-Based CO_2 Interpretation From 4D Sleipner Seismic Images. *Journal of Geophysical Research: Solid Earth, 126*(12), p.e2021JB022524.
- Li, D., Xu, K., Harris, J.M., & Darve, E. (2020). Coupled time-lapse full-waveform inversion for subsurface flow problems using intrusive automatic differentiation. *Water Resources Research, 56(8)*, p.e2019WR027032.
- Liu, M., & Grana, D. (2019). Accelerating geostatistical seismic inversion using TensorFlow: A heterogeneous distributed deep learning framework. *Computers & Geosciences, 124*, pp.37-45.

- Liu, M. (2022). Joint inversion of geophysical data for geologic carbon sequestration monitoring: a differentiable physics-informed deep learning model. [Source code]. https://github.com/theanswer003/JointInvDP
- Martin, D., & Estrin, G. (1967). Models of computations and systems—evaluation of vertex probabilities in graph models of computations. *Journal of the ACM (JACM), 14*(2), pp.281-299.
- Metz, B., Davidson, O., & De Coninck, H. eds. (2005). Carbon dioxide capture and storage: special report of the intergovernmental panel on climate change. *Cambridge University Press*.
- Mindlin, R.D. (1949). Compliance of elastic bodies in contact. *J. Appl. Mech., ASME 16*, 259–268.
- Raissi, M., Perdikaris, P., & Karniadakis, G.E. (2019). Physics-informed neural networks: A deep learning framework for solving forward and inverse problems involving nonlinear partial differential equations. *Journal of Computational physics, 378*, pp.686-707.
- Rall, L.B. (1981). Automatic differentiation: Techniques and applications. *Berlin, Heidelberg: Springer Berlin Heidelberg*.
- Rasht-Behesht, M., Huber, C., Shukla, K., & Karniadakis, G.E. (2022). Physics-Informed Neural Networks (PINNs) for Wave Propagation and Full Waveform Inversions. *Journal of Geophysical Research: Solid Earth, 127*(5), p.e2021JB023120.
- Rasmussen, A.F., Sandve, T.H., Bao, K., Lauser, A., Hove, J., Skaflestad, B., Klöfkorn, R., Blatt, M., Rustad, A.B., Sævareid, O., & Lie, K.A. (2021). The open porous media flow reservoir simulator. *Computers & Mathematics with Applications, 81*, pp.159-185.
- Rubino, J.G., Velis, D.R., & Sacchi, M.D. (2011). Numerical analysis of wave-induced fluid flow effects on seismic data: Application to monitoring of CO_2 storage at the Sleipner field.

Journal of Geophysical Research: Solid Earth, 116(B3).

- Tang, H., Fu, P., Jo, H., Jiang, S., Sherman, C.S., Hamon, F., Azzolina, N.A., & Morris, J.P. (2022). Deep Learning-Accelerated 3D Carbon Storage Reservoir Pressure Forecasting Based on Data Assimilation Using Surface Displacement from InSAR. *arXiv preprint* arXiv:2201.08543.
- Tveit, S., Mannseth, T., Park, J., Sauvin, G., & Agersborg, R. (2020). Combining CSEM or gravity inversion with seismic AVO inversion, with application to monitoring of large-scale CO_2 injection. *Computational Geosciences, 24*(3), pp.1201-1220.
- Vo, H.X., & Durlofsky, L.J. (2014). A new differentiable parameterization based on principal component analysis for the low-dimensional representation of complex geological models. *Mathematical Geosciences, 46*(7), pp.775-813.
- Yilmaz, Ö. (2001). Seismic data analysis (Vol. 1, p. 1809). *Tulsa: Society of exploration geophysicists*.
- Zhu, W., Xu, K., Darve, E., Biondi, B., & Beroza, G.C. (2022). Integrating deep neural networks with full-waveform inversion: Reparameterization, regularization, and uncertainty quantification. *Geophysics, 87*(1), pp.R93-R109.